Intensity Mapping of Hα, Hβ, [OII], and [OIII] Lines at z < 5

Gong, Yan; Cooray, Asantha; Silva, Marta B.; Zemcov, Michael; Feng, Chang; Santos, Mario G.; Dore, Olivier; Chen, Xuelei

Published in:
The Astrophysical Journal

DOI:
10.3847/1538-4357/835/2/273

Publication date:
2017

The Astrophysical Journal, 835:273 (14pp), 2017 February 1 doi:10.3847/1538-4357/835/2/273

Intensity Mapping of Hα, Hβ, [O II], and [O III] Lines at $z < 5$

Yan Gong[1,2], Asantha Cooray[2], Marta B. Silva[3], Michael Zemcov[4,5], Chang Feng[2], Mario G. Santos[6,7], Olivier Dore[5,8], and Xuelei Chen[1,9,10]
[1] Key Laboratory for Computational Astrophysics, National Astronomical Observatories, Chinese Academy of Sciences, 20A Datun Road, Beijing 100012, China
[2] Department of Physics & Astronomy, University of California, Irvine, CA 92697, USA
[3] Kapteyn Astronomical Institute, University of Groningen, Landleven 12, 9747AD Groningen, the Netherlands
[4] Center for Detectors, School of Physics and Astronomy, Rochester Institute of Technology, Rochester, NY 14623, USA
[5] NASA Jet Propulsion Laboratory, California Institute of Technology, 4800 Oak Grove Drive, MS 169-215, Pasadena, CA 91109, USA
[6] Physics Department, University of the Western Cape, Cape Town 7535, South Africa
[7] SKA SA, The Park, Park Road, Cape Town 7405, South Africa
[8] California Institute of Technology, MC 249-17, Pasadena, CA 91125, USA
[9] University of Chinese Academy of Sciences, Beijing 100049, China
[10] Center of High Energy Physics, Peking University, Beijing 100871, China
Received 2016 October 27; revised 2016 December 18; accepted 2016 December 22; published 2017 February 1

Abstract

Intensity mapping is becoming a useful tool to study the large-scale structure of the universe through spatial variations in the integrated emission from galaxies and the intergalactic medium. We study intensity mapping of the Hα 6563 Å, [O III] 5007 Å, [O II] 3727 Å, and Hβ 4861 Å lines at $0.8 \leqslant z \leqslant 5.2$. The mean intensities of these four emission lines are estimated using the observed luminosity functions (LFs), cosmological simulations, and the star formation rate density (SFRD) derived from observations at $z \lesssim 5$. We calculate the intensity power spectra and consider the foreground contamination of other lines at lower redshifts. We use the proposed NASA small explorer SPHEREx (the Spectro-Photometer for the History of the universe, Epoch of Reionization, and Ices Explorer) as a case study for the detectability of the intensity power spectra of the four emission lines. We also investigate the cross-correlation with the 21 cm line probed by the Canadian Hydrogen Intensity Mapping Experiment (CHIME), Tianlai experiment and the Square Kilometer Array (SKA) at $0.8 \leqslant z \leqslant 2.4$. We find both the auto and cross power spectra can be well measured for the Hα, [O III] and [O II] lines at $z \lesssim 3$, while it is more challenging for the Hβ line. Finally, we estimate the constraint on the SFRD from intensity mapping, and find we can reach an accuracy higher than 7% at $z \lesssim 4$, which is better than with the usual method of measurements using the LFs of galaxies.

Key words: cosmology: theory – diffuse radiation – intergalactic medium – large-scale structure of universe

1. Introduction

Measurements of the large-scale structure (LSS) of the universe are essential for studies of dark matter, dark energy and other aspects of cosmology. Ordinary galaxy surveys focus on individual galaxies and map the space distribution object by object, thereby tracing the LSS of underlying dark matter. These surveys have allowed successful measurements of cosmic LSS at low redshifts with $z \lesssim 1$, e.g., the Sloan Digital Sky Surveys (SDSS).[11] At higher redshifts, galaxies become fainter and smaller on average, making individual detections challenging. However, the key to important questions regarding dark energy, galaxy evolution, and cosmic LSS lies at $1 \lesssim z \lesssim 3$ and even higher redshifts. A method that does not rely on individual source detection is necessary to make progress.

Intensity mapping of atomic and molecular lines provides a suitable tool for cosmological study. It can probe faint and remote galaxies with large spatial volume in an acceptable observation time, and does not need to resolve individual sources. Since the emission lines of atoms and molecules are tightly coupled to the stellar content and environment of the host galaxy, intensity mapping of emission lines can also provide statistical information about the star formation rate (SFR) and other galaxy properties.

Recently, intensity mapping of atomic and molecular emission lines such as CO, [C II], Lyα, H_2, etc., for studying the epoch of reionization (EoR) and the epochs before and after EoR at high redshifts, have been discussed (Visbal & Loeb 2010; Carilli 2011; Gong et al. 2011b, 2012, 2013, 2014; Lidz et al. 2011; Silva et al. 2013, 2015; Pullen et al. 2014; Uzgil et al. 2014; Fonseca et al. 2016). These works indicate that intensity mapping of atomic and molecular emission lines is a powerful tool for studying the high-z universe, and it complements the method of using low-frequency radio experiments that measure the 21 cm flip-spin line from neutral hydrogen.

In this work, we study intensity mapping of four optical luminous lines, i.e., Hα 6563 Å, [O III] 5007 Å, [O II] 3727 Å and Hβ 4861 Å, in the redshift range $0.8 \leqslant z \leqslant 5.2$. We investigate the mean intensities of the four lines, and estimate the intensity power spectra at different redshifts. Foreground contamination from other lines at lower redshifts is also discussed, which is an important issue in intensity mapping surveys. In order to evaluate the detectability of the power spectra in a real measurement, we study the proposed space telescope Spectro-Photometer for the History of the universe, Epoch of Reionization, and Ices Explorer (SPHEREx)[12], and estimate the errors and signal-to-noise ratio (S/N) for the intensity power spectra at $0.8 \leqslant z \leqslant 5.2$. The cross-correlation

[11] http://www.sdss.org/

[12] http://spherex.caltech.edu/

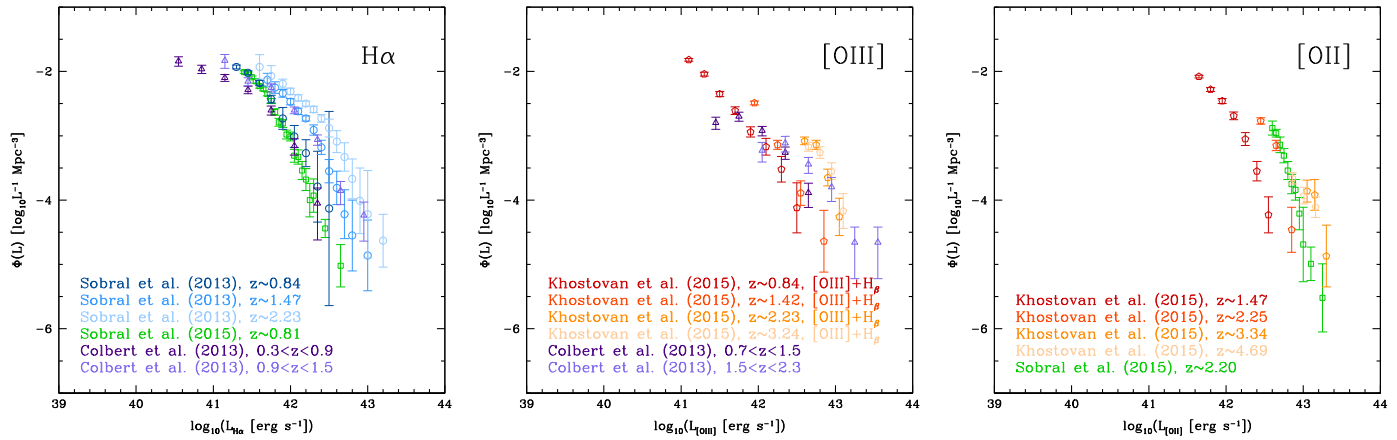

Figure 1. Observed luminosity functions of Hα, [O III] and [O II] used in the estimation of mean intensity (Colbert et al. 2013; Sobral et al. 2013, 2015; Khostovan et al. 2015). These LFs are not corrected for dust extinction. The Hα LFs in Sobral et al. (2013) have had dust extinction of $A_{\rm H\alpha} = 1$ mag reapplied to match the other data sets. The LFs in Khostovan et al. (2015) are for [O III]+Hβ instead of [O III] only.

of these lines with the hydrogen 21 cm line is also studied at $0.8 \leqslant z \leqslant 2.4$. The cross-correlation can effectively reduce the foreground line contamination and instrument noise, and offers a reliable way to extract the signal. We discuss two 21 cm experiments in our work, the Canadian Hydrogen Intensity Mapping Experiment (CHIME[13]) and Chinese experiment "Tianlai".[14] Finally, we explore the constraint on the star formation rate density (SFRD) at different redshifts available from this intensity mapping survey.

This paper is organized as follows: in Section 2, we estimate the mean intensities of the lines at $z < 6$ using three different methods. In Section 3, we calculate the intensity power spectra of the four lines at $0.8 \leqslant z \leqslant 5.2$ using a halo model. In Section 4, we discuss foreground contamination and the detectability of the line intensity power spectra with the SPHEREx experiment. In Section 5, we explore the cross correlation with the 21 cm line measured by CHIME, Tianlai experiments, and the Square Kilometer Array (SKA). In Section 6, the constraint of the SFRD at different redshifts is predicted with the intensity mapping measurements. In this paper, we adopt the flat ΛCDM model with $\Omega_b = 0.046$, $\Omega_M = 0.27$, $\Omega_\Lambda = 0.73$, $h = 0.71$, $\sigma_8 = 0.81$ and $n_s = 0.96$ as the fiducial model.

2. Line Mean Intensity

In this section, we estimate the observed mean line intensities of Hα, [O III], [O II] and Hβ at $z < 5$. We make use of the observed luminosity functions (LFs), the SFRs calculated from simulations and the SFRD derived from observations to estimate the mean intensity for each line. The effect of dust extinction is also considered in our estimates.

2.1. Mean Intensity from LF

The direct way to estimate the mean intensity of an emission line is to use the observed line LFs. In Figure 1, we show the luminosity function data of Hα, [O III] and [O II] at different redshifts, and we adopt their fitting formulae in our calculation (Colbert et al. 2013; Sobral et al. 2013, 2015; Khostovan et al. 2015). These LFs are not corrected for dust extinction, since we are trying to derive the observed mean intensity for each line. The Hα LFs given in Sobral et al. (2013) have been corrected for dust extinction with $A_{\rm H\alpha} = 1$ mag, and we use the same extinction law and rescale these LFs back to include dust extinction effect. The LFs are fitted by the Schechter function (Schechter 1976)

$$\Phi(L)dL = \phi_*\left(\frac{L}{L_*}\right)^{\alpha}\exp\left(-\frac{L}{L_*}\right)\frac{dL}{L_*}, \quad (1)$$

where ϕ_*, α, and L_* are the free parameters obtained by fitting observational data. The observed mean intensity can then be estimated from

$$\bar{I}_\nu(z) = \int_{L_{\rm min}}^{L_{\rm max}} dL\ \Phi(L)\frac{L}{4\pi D_L^2}\,y(z)D_A^2. \quad (2)$$

Here we take $L_{\rm min} = 10^6\ L_\odot$ and $L_{\rm max} = 10^{12}\ L_\odot$, and D_L and D_A are the luminosity and comoving angular diameter distance, respectively. The factor $y(z) = dr/d\nu = \lambda_{\rm line}(1+z)^2/H(z)$, where r is the comoving distance, $\lambda_{\rm line}$ is the rest-frame wavelength of emission line, and $H(z)$ is the Hubble parameter at z. The uncertainty of $\bar{I}_\nu$ is evaluated from the uncertainties in the observed LFs for each line, which is based on the errors of the LF fitting parameters.

2.2. Mean Intensity from the SFR

The strengths of the Hα 6563Å, [O III] 5007 Å, [O II] 3727 Å and Hβ 4861 Å lines are tightly related to the SFR of galaxies, which provides another way to evaluate their mean intensities through the $L_{\rm line}$–SFR relation. The relations are given by (Kennicutt 1998; Ly et al. 2007; Gong et al. 2014)

$$\mathrm{SFR}(M_\odot\ \mathrm{yr}^{-1}) = (7.9 \pm 2.4) \times 10^{-42} L_{\rm H\alpha}, \quad (3)$$

$$\mathrm{SFR}(M_\odot\ \mathrm{yr}^{-1}) = (7.6 \pm 3.7) \times 10^{-42} L_{\rm [O\ III]}, \quad (4)$$

$$\mathrm{SFR}(M_\odot\ \mathrm{yr}^{-1}) = (1.4 \pm 0.4) \times 10^{-41} L_{\rm [O\ II]}. \quad (5)$$

For the Hβ line, we take the line ratio Hβ/H $\alpha = 0.35$ (Osterbrock & Ferland 2006), which is found to be in good agreement with observations and simulations, as we discuss later.

The SFR can be evaluated by two means, both of which are associated to the halo mass M. First, we derive the SFR(M) from the simulations in Guo et al. (2013). These Millennium

[13] http://chime.phas.ubc.ca/
[14] http://tianlai.bao.ac.cn/

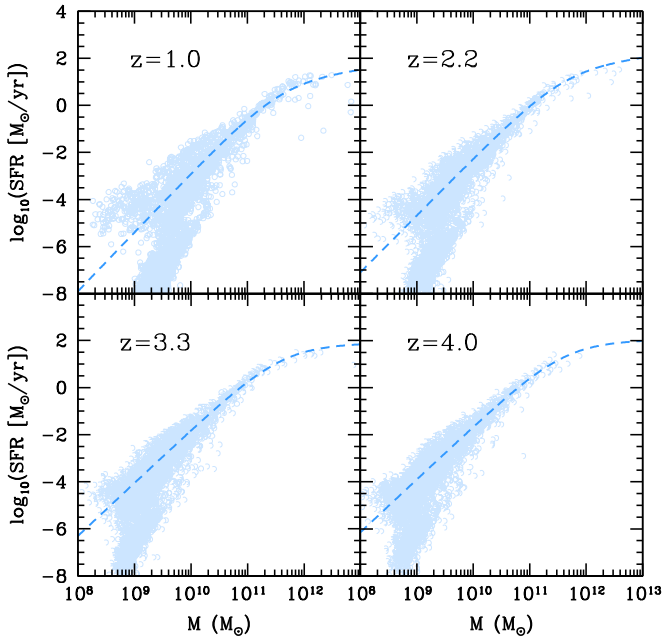

Figure 2. SFR derived from simulations in Guo et al. (2013). The SFR data are light blue circles and the best-fitting results are blue dashed curves. We find the uncertainties of the SFR increase for low-mass halos with $M < 10^{11}\ M_{\odot}$, and the star formation is quenched at $M < 10^{8}\ M_{\odot}$.

and Millennium II simulations are based on the first-year *Wilkinson Microwave Anisotropy Probe* (*WMAP*) results for a ΛCDM universe with cosmological parameters rescaled to be consistent with the seven-year *WMAP* data (Komatsu et al. 2011). A semi-analytic galaxy and star formation model is employed in the simulations, which is calibrated by SDSS data (Guo et al. 2013). We use the following formula to fit the SFR (M) at different redshifts

$$\mathrm{SFR}(M) = 10^{a}\left(\frac{M}{M_1}\right)^{b}\left(1+\frac{M}{M_2}\right)^{c}, \tag{6}$$

where a, b, c, M_1 and M_2 are free parameters. In Figure 2, as examples, we show the SFR(M) data (light blue circles) derived from the simulations and the best-fitting results (blue dashed curves) at $z = 1.0$, 2.2, 3.3, and 4.0. The fitting values of these parameters at $z = 1.0$, 1.4, 1.8, 2.2, 2.7, 3.3, 4.0, and 4.8 are listed in Table 1. We find the SFR becomes flat at $M \gtrsim 10^{12}$ $M_{\odot}$ for $z < 5$. The uncertainty of SFR-M increases for low-mass halos and there is almost no star formation for $M < 10^{8}\ M_{\odot}$.

We also derive the SFR(M) from observational results of the cosmic SFRD. Following Hopkins & Beacom (2006), we take the fitting formula given by (Cole et al. 2001)

$$\mathrm{SFRD}(z) = \frac{a+bz}{1+(z/c)^{d}}\ (M_{\odot}\ \mathrm{yr}^{-1}\,\mathrm{Mpc}^{-3}\,h), \tag{7}$$

where $a = 0.0118$, $b = 0.08$, $c = 3.3$ and $d = 5.2$ for the initial mass function proposed in Baldry & Glazebrook (2003). We also assess the SFRD(z) suggested by Madau & Dickinson (2014), and we find that the results derived from the two SFRDs are similar. As a theoretical discussion, we decide to take the SFRD given by Hopkins & Beacom (2006), since it seems more consistent with the mean intensities derived from both of the observed LFs and the simulations, as we discuss later. For simplicity, we assume the SFR is proportional to halo mass M, which is a good approximation for $M < 10^{12}\ M_{\odot}$ as shown in Figure 2. The SFR is given by

$$\mathrm{SFR}(M, z) = f_{*}(z)\frac{\Omega_b}{\Omega_M}\frac{1}{t_s}M, \tag{8}$$

where $t_s = 10^{8}$ years is the typical star formation timescale, and $f_{*}(z)$ is the star formation efficiency which can be determined by the relation $\mathrm{SFRD}(z) = \int dM\,(dn/dM)\mathrm{SFR}(M, z)$, where dn/dM is the halo mass function (Cooray & Sheth 2002).

With the SFR(M, z) estimated by simulations and observed SFRD(z), the luminosities $L(M, z)$ of Hα, [O III], [O II] and Hβ can be obtained by Equations (3)–(5), repectively. Then the mean intensity can be calculated from

$$\bar{I}_{\nu}(z) = \int_{M_{\mathrm{min}}}^{M_{\mathrm{max}}} dM\frac{dn}{dM}\frac{L_{\mathrm{line}}(M, z)}{4\pi D_{\mathrm{L}}^{2}}y(z)D_{\mathrm{A}}^{2}, \tag{9}$$

where $M_{\mathrm{min}} = 10^{8}\ M_{\odot}\ h^{-1}$ and $M_{\mathrm{max}} = 10^{13}\ M_{\odot}\ h^{-1}$ are the minimum and maximum halo masses we assume.

We note that this mean intensity is the intrinsic intensity without dust extinction, since it is directly derived from the SFR obtained by simulations and the SFRD(z) corrected for extinction. To account for the effect of dust extinction, we assume the mean dust extinctions, which are averaged over M_B magnitude, as $A_{\mathrm{H}\alpha} = 1.0$ mag, $A_{[\mathrm{O\,III}]} = 1.32$ mag, $A_{[\mathrm{O\,II}]} = 0.62$ mag, and $A_{\mathrm{H}\beta} = 1.38$ mag (Kennicutt 1998; Calzetti et al. 2000; Hayashi et al. 2013; Khostovan et al. 2015). Note that the values of $A_{[\mathrm{O\,III}]}$ and $A_{\mathrm{H}\beta}$ are based on standard $A_{\mathrm{H}\alpha} = 1.0$ mag, while $A_{[\mathrm{O\,II}]}$ is for $A_{\mathrm{H}\alpha} = 0.35$ mag, obtained by comparing with the SFRD results (Khostovan et al. 2015). When we estimate the uncertainty of the mean intensity $\bar{I}_{\nu}$, we consider both the uncertainties of the relation of L_{line}–SFR and the SFRD from observations for different redshifts.

2.3. Results of Mean Intensity

In Figure 3, we show the estimated mean intensities of Hα, [O III], [O II] and Hβ lines at $z < 5$. We find the mean intensities derived from the three methods (i.e., LFs, SFR simulations, and observed SFRD) are mainly consistent at the 1σ confidence level (C.L.), except that the results for Hα LFs at $z < 0.5$ are somewhat lower and the results from the simulations around $z = 4.8$ are slightly higher than the other two methods. As expected, the mean intensities follow the profile of SFRD(z) with a peak around $z = 2$. The intensity of the Hα line is stronger than the other lines at the same redshift, and vary from a few Jy sr^{-1} to ∼20–30 Jy sr^{-1} over the redshift range. The intensity of the [O III] line is comparable with that of Hα and has a larger uncertainty. The intensity of the [O II] line is lower than that of [O III], and we find that the [O II] intensity from the SFRD is in good agreement with the LF results over $1 < z < 5$. The Hβ intensity is the smallest among the four lines, and is almost one order of magnitude lower than that of the Hα line.

For the Hβ line, good measurements of Hβ LFs are not available for comparison, so we simply use $\mathrm{H}\beta/\mathrm{H}\alpha = 0.35$ to derive the Hβ intensity. In order to validate the results, we calculate the intensity of [O III]+Hβ and compare it with the results from observed [O III]+Hβ LFs in Khostovan et al. (2015). The result is shown in Figure 4. We find that the [O III] +Hβ intensity obtained from the SFRD matches the result of

Table 1
Fitting Parameters for the SFR(M) Derived from Simulations in Guo et al. (2013)

	$z = 1$	$z = 1.4$	$z = 1.8$	$z = 2.2$	$z = 2.7$	$z = 3.3$	$z = 4.0$	$z = 4.8$
a	−7.90	−7.70	−7.50	−7.10	−6.78	−6.30	−6.15	−5.90
b	2.50	2.49	2.49	2.42	2.36	2.25	2.25	2.25
c	−2.18	−2.18	−2.25	−2.10	−2.20	−2.20	−2.20	−2.20

Note. M_1 and M_2 in Equation (6) are fixed to be 1.0×10^8 and 4.0×10^{11} $M_\odot$, respectively, for all redshifts.

LFs very well, which indicates that the Hβ intensity we estimate is reasonable.

By comparing the intensity results from LFs, SFR simulations, and observed SFRD, we find that the intensities obtained by the SFRD(z) of Hopkins & Beacom (2006) are in good agreement with the other methods and convenient for theoretical estimation. Hence, we take the intensity results from the SFRD in our following discussion.

3. Line Intensity Power Spectrum

In this section, we estimate the 3D intensity power spectra for Hα, [O III], [O II] and Hβ lines at different redshifts. Since the emission lines come from galaxies that trace the distribution of underlying dark matter, the fluctuation of line intensity can be expressed by

$$\delta I_{\rm line} = \bar{b}_{\rm line}\, \bar{I}_{\rm line}\, \delta(\boldsymbol{x}), \tag{10}$$

where $\bar{I}_{\rm line}$ is the mean intensity we estimate in the last section, $\delta(\boldsymbol{x})$ is the over-density of the dark matter field at position $\boldsymbol{x}$, and $\bar{b}_{\rm line}$ is the weighted galaxy bias by the luminosity of the emission line, which is given by

$$\bar{b}_{\rm line}(z) = \frac{\int_{M_{\rm min}}^{M_{\rm max}} dM \frac{dn}{dM} L_{\rm line}\, b(M, z)}{\int_{M_{\rm min}}^{M_{\rm max}} dM \frac{dn}{dM} L_{\rm line}}, \tag{11}$$

where $b(M, z)$ is the halo bias (Sheth & Tormen 1999). We can then calculate the clustering power spectrum of the line that traces galaxy clustering as

$$P_{\rm line}^{\rm clus}(k, z) = \bar{b}_{\rm line}^{\,2}\, \bar{I}_{\rm line}^{2}\, P_{\delta\delta}(k, z). \tag{12}$$

Here $P_{\delta\delta}(k, z)$ is the matter power spectrum, and we use the halo model of Cooray & Sheth (2002) to calculate it. For simplicity, we ignore redshift distortion in this work, and only focus on the isotropic spatial fluctuations. At small scales, shot noise is the dominant term, which is due to the discrete distribution of galaxies. The shot-noise power spectrum for an emission line is given by

$$P_{\rm line}^{\rm shot}(z) = \int_{M_{\rm min}}^{M_{\rm max}} dM \frac{dn}{dM} \left[\frac{L_{\rm line}}{4\pi D_{\rm L}^2 y(z) D_{\rm A}^2}\right]^2. \tag{13}$$

For the result using the LFs, the terms dn/dM and dM are replaced by $\Phi(L)$ and dL, respectively. The total power spectrum is $P_{\rm line}^{\rm tot}(k, z) = P_{\rm line}^{\rm clus}(k, z) + P_{\rm line}^{\rm shot}(z)$.

In Figure 5, we show the power spectra of Hα, [O III], [O II], and Hβ lines at $z = 1.0 \pm 0.2$, 1.4 ± 0.2, 1.8 ± 0.2, 2.2 ± 0.2, 2.7 ± 0.3, 3.3 ± 0.3, 4.0 ± 0.4, and 4.8 ± 0.4 including the effects of dust extinction. We assume there is no evolution for the power spectra in each redshift interval. These power spectra also can be seen as the average power spectra over the corresponding redshift intervals, since we find that they have similar amplitudes and shapes to the average ones. As expected, the power spectra of the Hα line is higher than the other three lines at the same redshift, since its mean intensity is the largest. The power spectrum of [O III] is larger than [O II], and Hβ has the lowest power spectrum. We also find that, for all four lines, the amplitudes of the power spectra at $1 \lesssim z \lesssim 2.2$ are quite similar to one another, no matter the redshift. This is because the mean intensity for each line peaks at $z \sim 2$ and the bias in Equation (11) is larger at higher redshifts, which compensates for the decrease of the matter power spectrum at higher redshifts. However, at $z \gtrsim 2.2$, the line power spectra decrease quickly as the redshift increases, since the mean intensity and the matter power spectrum both decrease. The clustering power spectrum is about two orders of magnitude higher at $1 \lesssim z \lesssim 2.2$ than that at $z \sim 5$, while it is almost three orders of magnitude higher for the shot-noise power spectra at the same redshifts. As we discuss in the next section, this leads to large differences in the detectability of the lines as a function of redshift.

4. Detectability of the Lines

In this section, we study the detectability of the Hα, [O III], [O II], and Hβ lines. We first discuss contamination from the foreground lines at lower redshifts and the method of removal, and then explore the detectability of the four lines with the proposed SPHEREx experiment.

4.1. Contamination of Foreground Emission Lines

In an intensity mapping survey, the detected pixel volume (or voxel) is characterized by the space and frequency resolutions of the instrument, whose directions are perpendicular and parallel to the line of sight, respectively. Hence, the different emission lines at different redshifts at the same observed frequency can be mixed together in a voxel. This effect is particularly important for measuring an emission line at high redshift, as other luminous lines at longer wavelengths at lower redshifts can contaminate the line at the high redshift in which we are interested.

For the Hα 6563 Å line, there is no emission line at longer wavelengths that can provide considerable contamination at lower redshifts, and so it is a good tracer for studies of the SFRD and matter distribution in intensity mapping surveys. Here we ignore foreground contaminating lines for the Hα line. For [O III] 5007 Å, the main foreground line contaminant is the Hα line at lower redshifts. For the Hβ 4861 Å line, we consider both the low-z Hα and [O III] lines as foreground contaminants. The [O II] 3727 Å line has the shortest wavelength among the four luminous lines, so it can be contaminated by all the other three lines at lower redshifts.

Following Gong et al. (2014), the observed 3D power spectrum is the sum of the signal power spectrum and all the

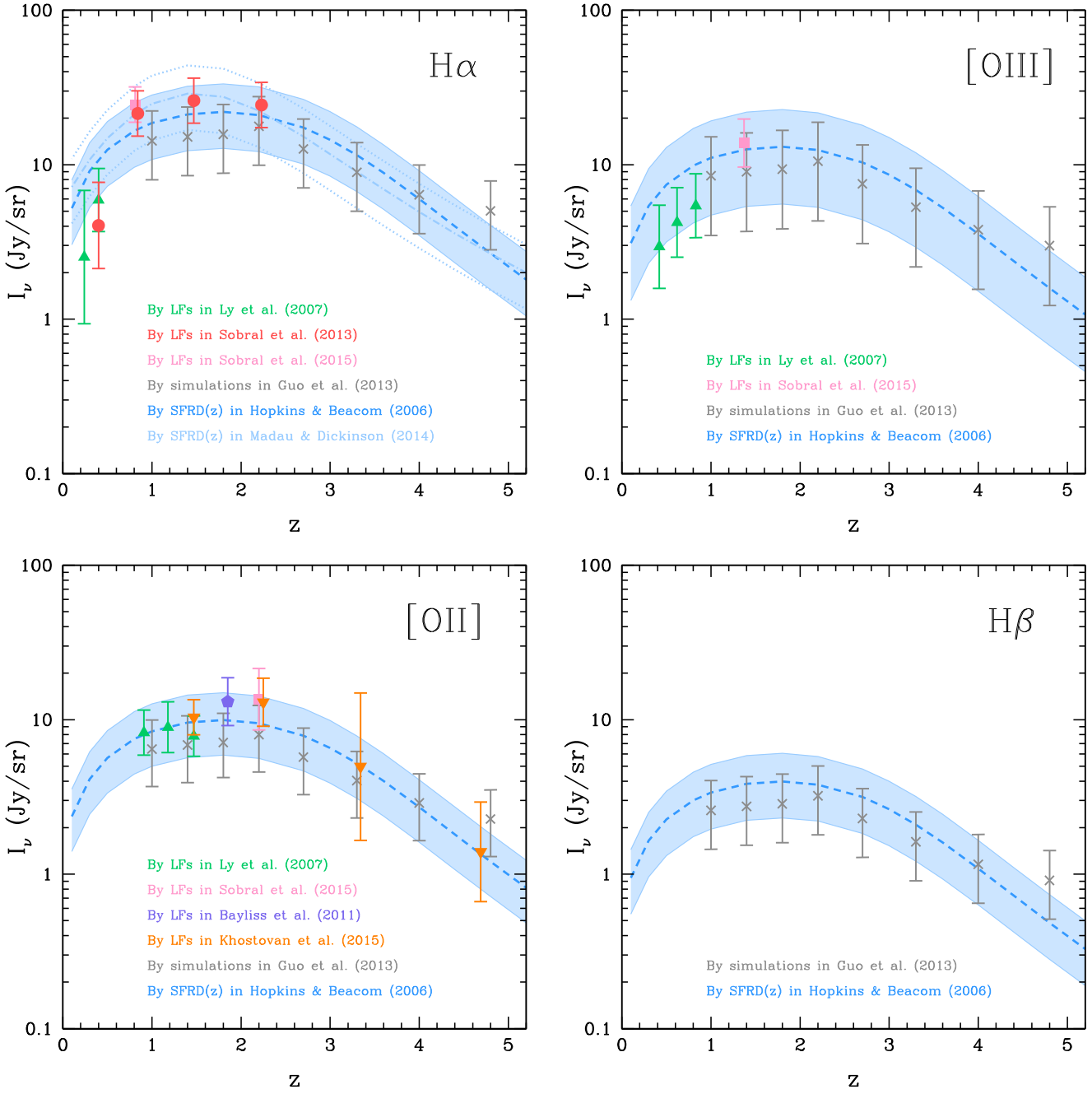

Figure 3. Mean intensities of Hα, [O III], [O II], and Hβ lines at $z < 5$, with no correction for dust extinction applied. The colored points are derived from observed LFs (Ly et al. 2007; Bayliss et al. 2011; Sobral et al. 2013, 2015; Khostovan et al. 2015). The gray crosses show the results from the simulations in Guo et al. (2013). The blue dashed curves with blue bands give the results of the SFRD in Hopkins & Beacom (2006) for mean intensities and uncertainties. For comparison, the light blue dashed–dotted and dotted curves denote the results with errors from the SFRD given by Madau & Dickinson (2014). We find the results from the three methods (i.e., LFs, SFR simulations and observed SFRD) are basically consistent with one another at the 1σ C.L.

projected foreground line power spectra

$$P_{\rm obs}(k, z) = P_s(k, z) + \sum_{i=1}^{N} P_f^{p,i}(k_f, z). \quad (14)$$

Here $k = \sqrt{k_\perp^2 + k_\parallel^2}$ is the 3D comoving wavenumber at the signal redshift z, where $k_\perp$ and $k_\parallel$ are the components which are perpendicular and parallel to the line of sight, respectively. The k_f denotes the wavenumber corresponding to k at the foreground redshift z_f, which is given by $k_f = \sqrt{A_\perp^2 k_\perp^2 + A_\parallel^2 k_\parallel^2}$. $A_\perp$ and $A_\parallel$ are the factors to transfer k to k_f, and we have $A_\perp = r_s/r_f$ and $A_\parallel = y_s/y_f$. The signal power spectrum $P_s(k, z)$ is the total power spectrum $P_{\rm line}^{\rm tot}(k, z)$ we derive in the last section. The projected foreground power spectrum $P_f^p(k_f, z)$ is the foreground power spectrum $P_f(k_f, z_f)$ projected to the signal redshift z, which takes the form

$$P_f^p(k_f, z) = A_\perp^2 A_\parallel P_f(k_f, z_f). \quad (15)$$

The factor $A_\perp^2 A_\parallel$ is caused by the expansion of volume elements when Fourier transforming the foreground correlation function at z_f to the projected foreground power spectrum

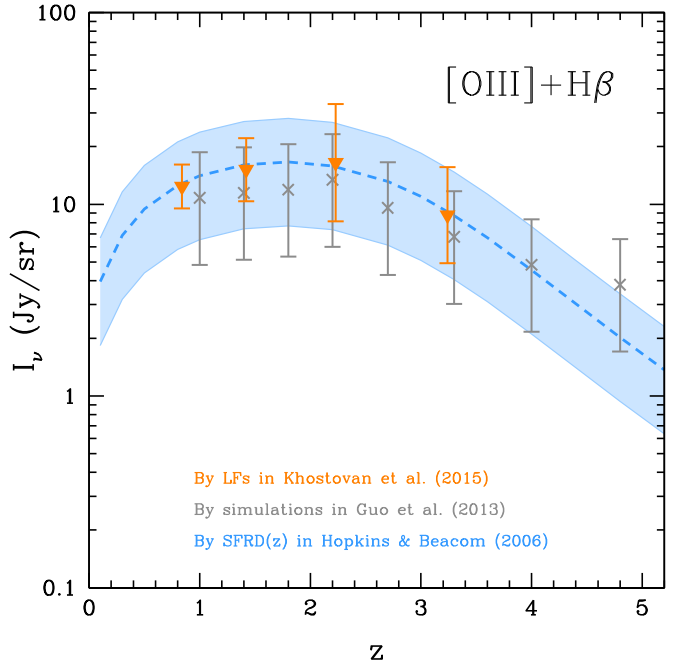

Figure 4. Mean intensity of [O III]+Hβ without corrections for dust extinction. We find the results are consistent with one another, indicating the relatively simple Hβ intensity estimate is reliable.

at z (Visbal & Loeb 2010; Gong et al. 2014). We find that the P_f^p is not isotropic along and perpendicular to the direction of line of sight, even after ignoring the redshift distortion effect, since the values of factors $A_\perp$ and $A_\parallel$ are different given that $z_s \neq z_f$. This effect can help us to identify and remove the foregrounds in intensity mapping surveys (Gong et al. 2014; Lidz & Taylor 2016). In this work, we focus on the 3D power spectrum, and we assume $k_1 = k_2 = k_\parallel$ where $\boldsymbol{k} = k_1\hat{\boldsymbol{i}} + k_2\hat{\boldsymbol{j}} + k_\parallel\hat{\boldsymbol{n}}$ and $k_\perp = \sqrt{k_1^2 + k_2^2}$.

Since the foreground lines at lower redshifts are relatively brighter than the signal line at higher redshift, the most direct way to remove the foregrounds is to mask the bright pixels above some flux level. In Figure 6, we show the intensity power spectrum of Hα, [O III], [O II], and Hβ lines at $z = 1.0 \pm 0.2$ and the foreground contaminating lines at lower redshifts. We show the power spectra of the foreground lines before and after applying a flux cut, which can suppress the foreground contamination about one order of magnitude below the signal. Note that there are several foreground lines that contaminate the [O II] and Hβ lines, so the flux cuts are for the total foregrounds. The flux cuts for each line at different redshifts within $0.8 \leqslant z \leqslant 5.2$ are shown in Table 2. We find the stronger lines, e.g., [O III] and [O II], have higher flux cuts than the weaker line Hβ at the same redshift, and the flux cuts decrease as the redshift increases, as expected. For the [O III] and [O II] lines, the flux cuts are similar at the same redshift, which varies from $\sim 10^{-22}$ to $\sim 10^{-24}$ W m^{-2}, while the Hβ flux cuts are about a factor of five lower than that of [O III] and [O II] at $z \lesssim 3$, and they become more and more similar at $z > 3$.

4.2. Detectability

Next, we discuss the detectability of the four lines at $0.8 \leqslant z \leqslant 5.2$ with the SPHEREx experiment. First, we need to estimate the variance of the intensity power spectrum. In a line intensity survey, the variance of the power spectrum at a given redshift is given by (e.g., Lidz et al. 2011; Gong et al. 2012; Uzgil et al. 2014)

$$\Delta P_{\rm line}(k)^2 = \frac{[P_{\rm line}(k) + P_N^{\rm line}(k)]^2}{N_m(k)}, \tag{16}$$

where $P_{\rm line}$ is the line intensity power spectrum we derived in the last section that denotes the cosmic variance term, and $P_N^{\rm line}(k)$ is the noise power spectrum that depends on the instrument and takes the form

$$P_N^{\rm line}(k) = \frac{V_{\rm pix}\,\sigma_{\rm pix}^2}{t_{\rm pix}}. \tag{17}$$

Here $\sigma_{\rm pix}^2/t_{\rm pix}$ denotes the squared instrument thermal noise per survey pixel, where $t_{\rm pix}$ is the integration time per pixel, and $V_{\rm pix}$ is the pixel volume. $N_m(k)$ is the number of Fourier modes in an interval Δk at k in the upper-half wavenumber plane. In principle, it can be evaluated by

$$N_m(k) = 2\pi k^2 \Delta k\,\frac{V_{\rm S}}{(2\pi)^3}, \tag{18}$$

where $V_{\rm S}$ is the total survey volume. Note that there can be a large discrepancy between the real N_m and the estimated one from Equation (18), especially at large k. In our calculation, we count the modes explicitly to determine N_m in each Δk. The S/N of the intensity power spectrum then can be derived by

$$\mathrm{S/N} = \sqrt{\sum_{k\ \rm bin}\left[\frac{P_{\rm line}(k)}{\Delta P_{\rm line}(k)}\right]^2}. \tag{19}$$

In order to investigate the detectability of the intensity power spectra of the four lines, we take the SPHEREx experiment as an example to estimate the error and S/N. SPHEREx is a proposed space telescope with a diameter of 20 cm, and has four bands which cover 0.75–1.32, 1.32–2.34, 2.34–4.12, and 4.12–4.83 μm, respectively. The frequency resolution of the first three bands is $R = 41.5$, and $R = 150$ in the fourth band. In our study, only the first three bands are used in the discussion for $z < 5$. We assume a deep SPHEREx survey with a total survey area of 200 deg^2 and a beam size 6.2×6.2 arcsec^2, which has repeated observations and can provide a data set ideal for intensity mapping (Dore et al. 2015).

In Figure 6, we show the estimated detection errors and S/N for the clustering power spectra of the Hα, [O III], [O II], and Hβ lines at $z = 1 \pm 0.2$. We find the S/N of Hα, [O III], [O II] lines are S/N > 18, which can be easily measured by SPHEREx, but the S/N of Hβ is low (S/N $\simeq$ 3) and difficult to detect. In Table 2, we list the S/N for each line at different redshifts. We can see that the Hα has S/N $\simeq$ 7 even at $z \sim 4$, and the S/Ns of [O III] and [O II] lines also are as high as S/N $\simeq$ 12 and 8 at $z \sim 3$, respectively. This indicates that SPHEREx can provide precision measurements of the intensity power spectra of Hα, [O III] and [O II] lines at $z \lesssim 3$. However, the S/N of the Hβ line is less than 3 at all redshifts, which is challenging to measure accurately.

In Figure 7, we show the total number of sources for each line, whose flux $f_{\rm line}$ is greater than a given value, in a survey voxel of SPHEREx at $z = 1.0 \pm 0.2$. In Table 2, we list the percent of voxels removed above these flux cuts for each line at

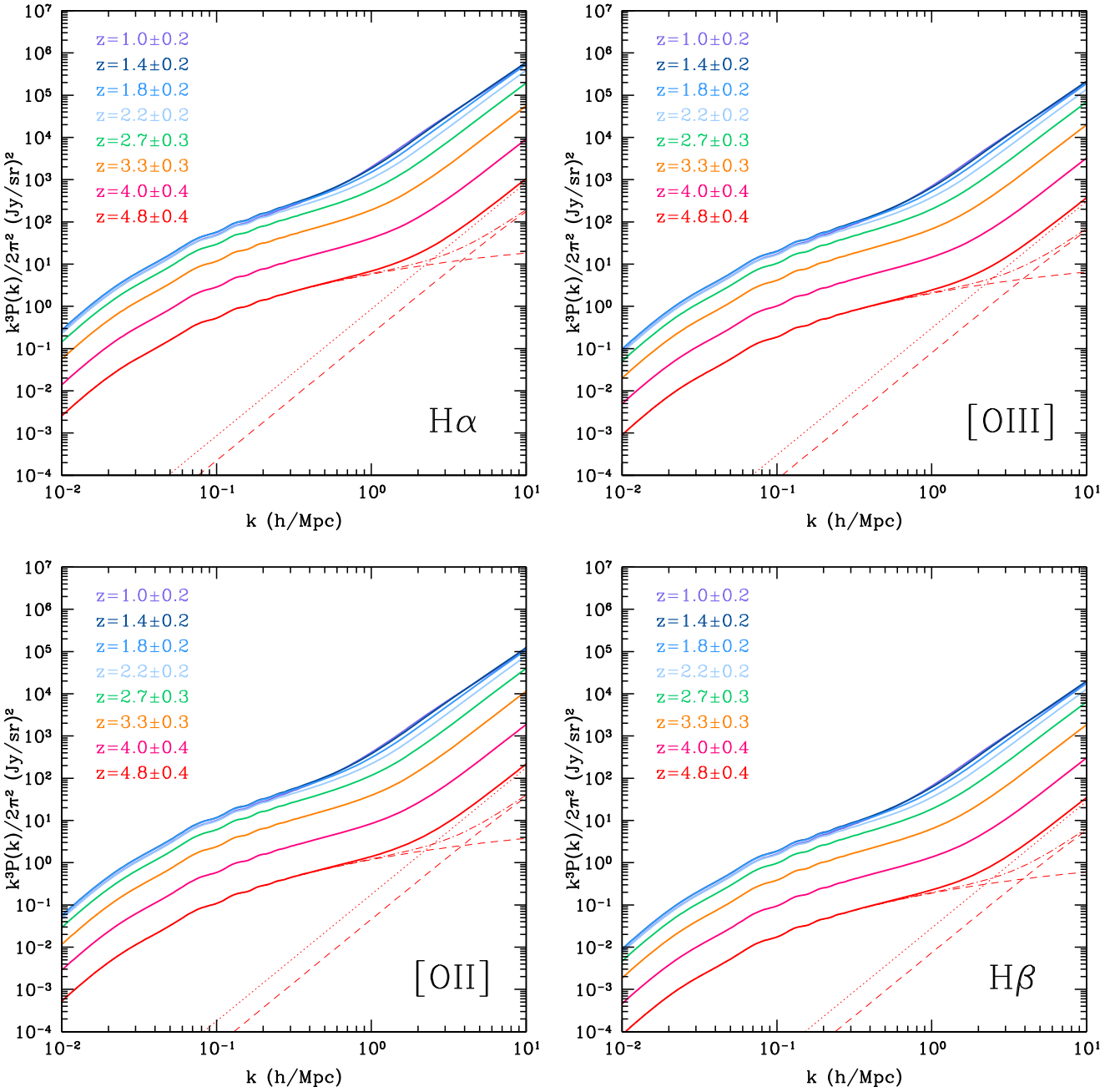

Figure 5. Intensity power spectra of Hα, [O III], [O II], and Hβ lines at different redshift ranges in $0.8 \leqslant z \leqslant 5.2$. These power spectra have included the dust extinction effect. The dashed curves show the 1-halo and 2-halo terms for $z = 4.8 \pm 0.4$, the dashed–dotted lines are the clustering power spectra, and the dotted lines are the shot-noise power spectra.

different redshifts. We find there are about 3% voxels for the [O III] and [O II] lines at $z = 1.0 \pm 0.2$ that need to be masked, and it is about 12% for Hβ line. The percent of removed voxels increase quickly as the redshift increases, and about 55%, 67%, and 87% for [O III], [O II], and Hβ at $z = 4.8 \pm 0.4$, respectively. For the Hβ line, we find the number of Hβ sources is comparable to that of foreground contaminates, even after performing the flux cut. This indicates that it is quite challenging to measure Hβ fluctuations with SPHEREx. For [O III] and [O II] lines in the range $z \lesssim 3$ with relatively high S/N > 3, the masked voxels are less than 10% and 30% for [O III] and [O II], respectively. This implies SPHEREx is capable of precisely measuring the intensity power spectra of the [O III] and [O II] lines at $z \lesssim 3$ with relatively small masked voxel fraction. Of course, the Hα line is the best observable with the strongest intensity and has no considerable foreground line contamination.

The contamination of continuum emission from galaxies and the recently proposed intrahalo light (IHL) also needs to be considered (Cooray et al. 2012b; Zemcov et al. 2014; Mitchell-Wynne et al. 2015; Silva et al. 2015; Yue et al. 2015). We find that the total mean intensity and power spectrum of the continuum emission can be larger than those of the four optical lines by two orders of magnitude. However, since the spectrum of the continuum emission is expected to be smooth, we can remove it in the observed 3D spectral line data cube by fitting polynomials (or other forms) as a function of frequency along different lines of sight (see e.g., Yue

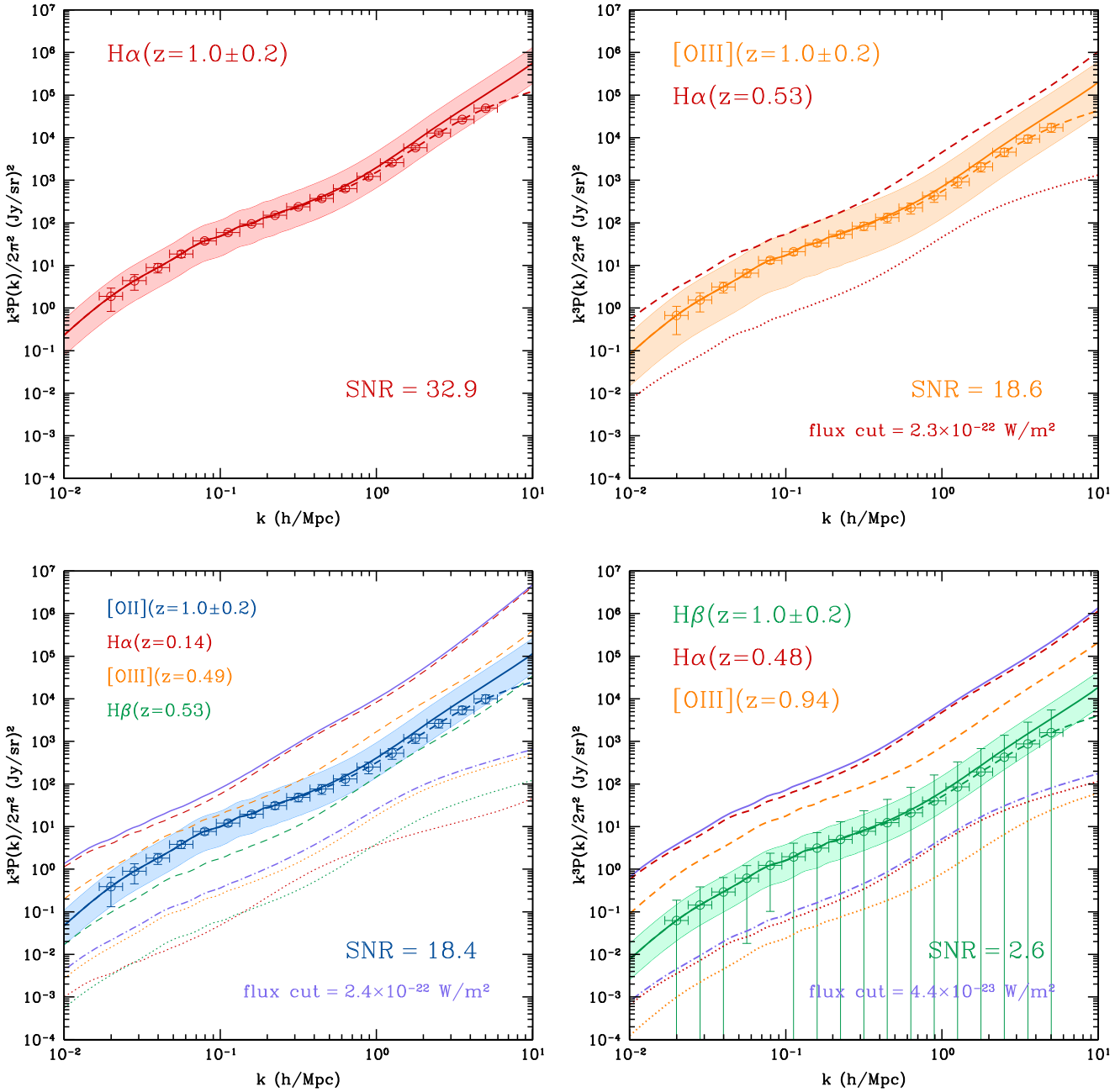

Figure 6. Intensity power spectra of Hα, [O III], [O II], and Hβ lines at $z = 1.0 \pm 0.2$ with the foreground contaminants. Upper left: the Hα power spectrum; there are no bright foreground lines that can affect the Hα signal. The solid and dashed curves denote the total and clustering power spectra, respectively. Upper right: the [O III] line contaminated by the low-z Hα line. The red dashed line is the projected foreground $P^p_{\rm H\alpha}$, and red dotted line denotes the $P^p_{\rm H\alpha}$ after a flux cut at 2.3×10^{-22} W m^{-2}. Lower left: the [O II] line contaminated by foreground Hα, [O III] and Hβ lines. The purple solid and dashed–dotted curves are the sum of the foreground lines before and after a flux cut at 2.4×10^{-22} W m^{-2}. Lower right: the Hβ line contaminated by low-z Hα and [O III] lines. We also show the error bars and S/N of the clustering power spectrum for each signal line for the SPHEREx experiment.

et al. 2015). This process does not affect the flux cuts and S/Ns significantly, and we will discuss it in detail in our future work with simulations. In addition, the contamination of zodiacal light should be small for the line power spectrum. This is because the spatial distribution of zodiacal light is relatively smooth with small fluctuations (Zemcov et al. 2014; Arendt et al. 2016), and the 200 deg^2 SPHEREx deep survey is planning to observe at the north and south ecliptic poles, where the zodiacal light is much fainter than that at low ecliptic latitudes.

5. Cross-correlation with the 21 cm Line

In order to remove foreground contamination, we can also cross-correlate different lines at the same redshift. Since the signals at the same redshift trace the same matter distribution while the foreground lines at different redshifts do not, cross-correlation can effectively reduce the foreground contamination. The direct cross-correlations can be performed between two lines of Hα, [O III], [O II], and Hβ. In principle, the value of the S/N for the cross power spectrum should be the geometric mean of the S/Ns of the auto power spectra for the two cross lines in the same

Table 2
S/Ns, Flux Cuts, and Percentages of Removed Pixels for Hα, [O III], [O II], and Hβ Line Intensity Mapping at $0.8 \leqslant z \leqslant 5.2$

Line		$z \sim 1.0$	$z \sim 1.4$	$z \sim 1.8$	$z \sim 2.2$	$z \sim 2.7$	$z \sim 3.3$	$z \sim 4.0$	$z \sim 4.8$
Hα	S/N	32.9	44.0	33.6	29.4	39.6	20.0	7.1	1.3
	flux cut (W m^{-2})	...	...	...	...	...	...	...	...
	% of removed pix.	...	...	...	...	...	...	...	...
[O III]	S/N	18.6	13.0	19.7	14.4	11.5	4.8	2.6	0.5
	flux cut (W m^{-2})	2.3×10^{-22}	1.4×10^{-22}	8.4×10^{-23}	6.0×10^{-23}	2.4×10^{-23}	6.8×10^{-24}	2.8×10^{-24}	1.3×10^{-24}
	% of removed pix.	3%	4%	5%	6%	10%	21%	42%	55%
[O II]	S/N	18.4	11.4	8.2	6.4	8.4	3.2	0.8	0.1
	flux cut (W m^{-2})	2.4×10^{-22}	8.6×10^{-23}	4.0×10^{-23}	2.5×10^{-23}	9.9×10^{-24}	4.6×10^{-24}	2.4×10^{-24}	9.9×10^{-25}
	% of removed pix.	3%	5%	9%	20%	32%	43%	53%	67%
Hβ	S/N	2.6	1.8	2.9	2.1	1.4	0.5	0.3	<0.1
	flux cut (W m^{-2})	4.4×10^{-23}	2.6×10^{-23}	1.3×10^{-23}	9.2×10^{-24}	5.2×10^{-24}	3.0×10^{-24}	1.6×10^{-24}	8.8×10^{-25}
	% of removed pix.	12%	15%	21%	27%	38%	48%	65%	87%

intensity survey. As a result, it is convenient to predict the S/N of cross power spectra between the four lines for SPHEREx experiment. We could also consider cross-correlating the intensity power spectrum with optical galaxy surveys (Lidz & Taylor 2016). In this work, we focus on the cross-correlation of the four lines probed by SPHEREx with the hydrogen hyperfine-structure 21 cm line measured by the CHIME and Tianlai experiments.

At low redshifts after the EoR, neutral hydrogen mainly resides in galaxies. Similar to the emission lines discussed above at $z < 5$, the 21 cm line emitted by neutral hydrogen also traces the distribution of galaxies and matter in the universe. As a result, the 21 cm line can correlate with optical lines at the same redshift. The clustering cross power spectrum is given by

$$P_{\rm cross}^{\rm clus}(k, z) = \bar{b}_{21\,\rm cm}\bar{b}_{\rm line}\bar{T}_{21\,\rm cm}\bar{T}_{\rm line}\,P_{\delta\delta}(k, z), \quad (20)$$

where $\bar{b}_{21\,\rm cm}$ and $\bar{T}_{21\,\rm cm}$ are the bias and mean brightness temperature of the 21 cm line, respectively (Gong et al. 2011b). $\bar{T}_{\rm line}$ is the mean brightness temperature of the four optical lines converted from the mean intensity $\bar{I}_{\rm line}$ by the Rayleigh–Jeans law. The $\bar{b}_{21\,\rm cm}$ is expressed by

$$\bar{b}_{21\,\rm cm}(z) = \frac{\int_{M_{\rm min}}^{M_{\rm max}} dM \frac{dn}{dM} M_{\rm H\,I}\, b(M, z)}{\rho_{\rm H\,I}}, \quad (21)$$

where $M_{\rm H\,I}(M, z)$ is the neutral hydrogen mass given by the fitting results of simulations in Gong et al. (2011a), and $\rho_{\rm H\,I} = \int dM\,(dn/dM) M_{\rm H\,I}$ is the mass density of neutral hydrogen. The mean 21 cm temperature can be estimated by (Chang et al. 2010)

$$\bar{T}_{21\,\rm cm}(z) = 248\left(\frac{\Omega_{\rm H\,I}}{10^{-3}}\right)\left(\frac{h}{0.73}\right)\left(\frac{1+z}{1.8}\right)^{0.5} \left[\frac{\Omega_M + \Omega_\Lambda(1+z)^{-3}}{0.37}\right]^{-0.5} \mu{\rm K}. \quad (22)$$

Here $\Omega_{\rm H\,I} = \rho_{\rm H\,I}/\rho_c$ where ρ_c is the critical density. We estimate the cross shot-noise term by

$$P_{\rm cross}^{\rm shot}(z) = \int_{M_{\rm min}}^{M_{\rm max}} dM \frac{dn}{dM}\left[\frac{L_{\rm line}}{4\pi D_{\rm L}^2} y(z) D_{\rm A}^2\right] \times \left(\bar{T}_{21\,\rm cm}\frac{M_{\rm H\,I}}{\rho_{\rm H\,I}}\right), \quad (23)$$

and the 21 cm shot-noise power spectrum is given by

$$P_{21\,\rm cm}^{\rm shot}(z) = \int_{M_{\rm min}}^{M_{\rm max}} dM \frac{dn}{dM}\left(\bar{T}_{21\,\rm cm}\frac{M_{\rm H\,I}}{\rho_{\rm H\,I}}\right)^2. \quad (24)$$

Then the total cross power spectrum is $P_{\rm cross}^{\rm tot} = P_{\rm cross}^{\rm clus} + P_{\rm cross}^{\rm shot}$. We also calculate the cross-correlation coefficient r, and find that r is always greater than 0.8 and varies from ∼0.8 to ∼1 as k becomes smaller.

In order to explore the detectability of the cross power spectrum, we also need to estimate the noise power spectrum given by the instruments, and we take the CHIME and Tianlai 21 cm experiments as examples. The CHIME and Tianlai experiments are radio interferometers with parabolic cylinder reflectors. The goal of CHIME and Tianlai is to measure the baryon acoustic oscillation (BAO) in the large-scale structure of the universe as traced by the 21 cm line from galaxies, and from such measurements to extract the properties of dark energy. Both of the experiments cover large sky fractions and redshift ranges to obtain accurate measurements of the 21 cm power spectrum and BAO features. The design parameters of these instruments can be found in Table 3.

We estimate the variance of the cross noise power spectrum at a given redshift by (e.g., Gong et al. 2012; Lidz & Taylor 2016)

$$(\Delta P_{\rm cross})^2 = \frac{P_{\rm cross}^2 + (P_{\rm line} + P_N^{\rm line})(P_{21\,\rm cm} + P_N^{21\,\rm cm})}{2\,N_m^{\rm cross}(k)}, \quad (25)$$

where $P_{\rm cross}$, $P_{\rm line}$ and $P_{21\,\rm cm}$ are the intensity power spectra of cross, the four lines, and 21 cm, respectively. The cross power spectrum can arise from both clustering and total power spectra depending on the regime of interest. The $N_m^{\rm cross}(k)$ is the number of modes in a k bin, and we count the modes explicitly to derive it from the smaller survey volume and larger voxel in the two different surveys. $P_N^{21\,\rm cm}$ is the noise power spectrum of the 21 cm line, which can be derived from the CHIME and Tianlai experiments, and it is given by (McQuinn et al. 2006)

$$P_N^{21\,\rm cm} = r_c^2\, y(z)\frac{\lambda^2\, T_{\rm sys}^2}{A_e\, t_k}. \quad (26)$$

Here r_c is the comoving distance, A_e is the effective area of an antenna, and $T_{\rm sys}$ is the system temperature. The

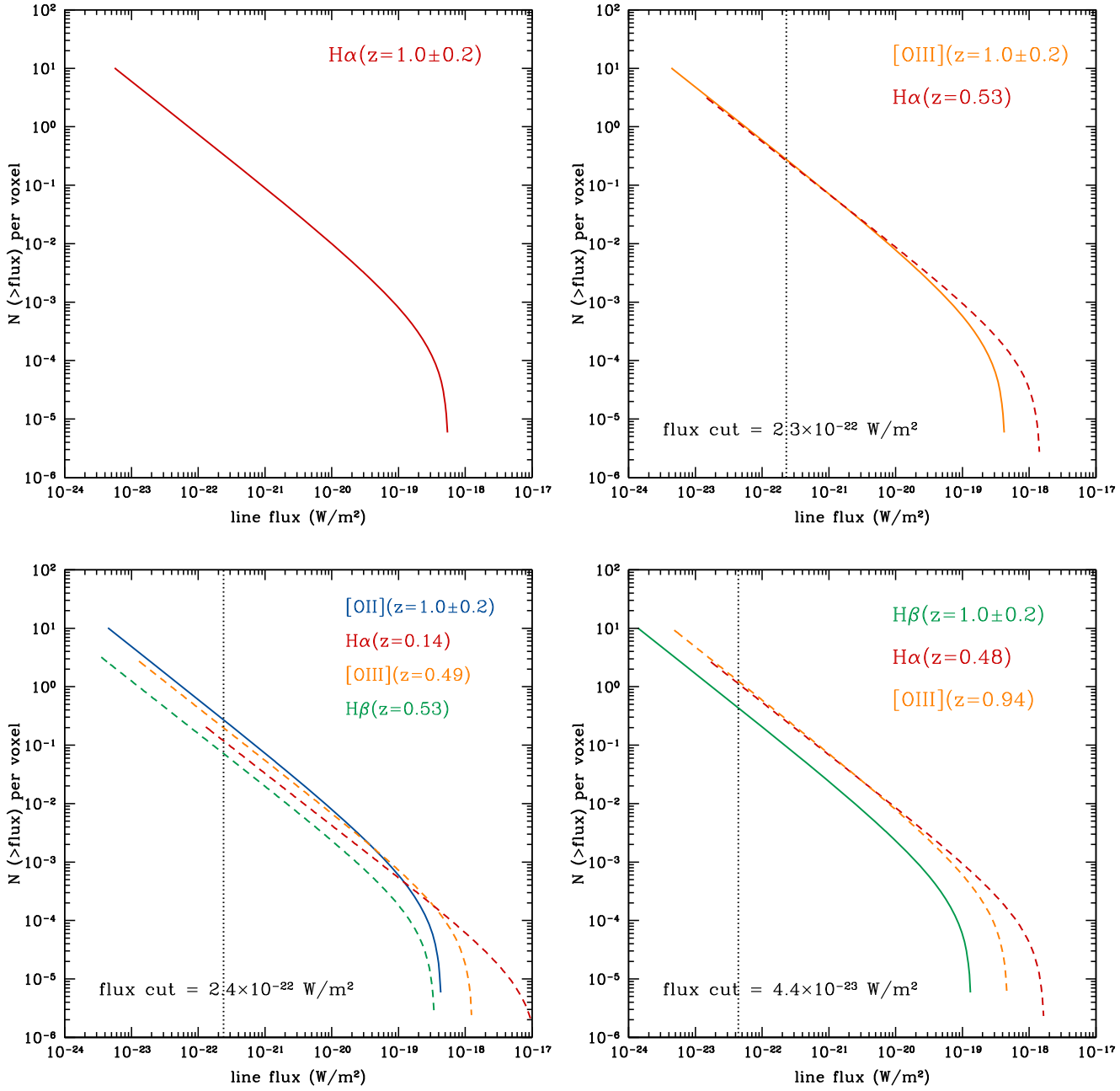

Figure 7. Total number of sources in a SPHEREx survey voxel whose flux is greater than a given value. The solid and dashed curves denote the number of signal and foreground lines, respectively. The flux cuts listed in Table 2 are shown by vertical dotted lines.

Table 3
Design Parameters for the CHIME and Tianlai Experiments We Use

	CHIME	Tianlai	Unit
Survey area A_s	10,000	10,000	deg^2
Total int. time $t_{\rm tot}$	10^4	10^4	hr
Total bandwidth	400–800	400–1420	MHz
Redshift range	0.8–2.5	0.0–2.5	⋯
Sys. Temp. $T_{\rm sys}$	50	50	K
FoV N-S	∼150	∼150	deg
FoV E-W	∼1.9	∼1.6	deg
Cylinder size	100 × 20	120 × 15	m^2
Num. of cylinders	5	8	⋯
Tot. Collecting area	10,000	14,400	m^2
Num. of feeds	256 × 5	275 × 8	⋯
Freq. resolution $\Delta\nu$	∼1	∼0.1	MHz

$t_k = t_0 (A_e/\lambda^2) n(\mu_\perp)$ is the average observation time for a mode k, where t_0 is the total integration time and $n(\mu_\perp)$ is the number density of the baselines. $\mu_\perp = k\,\sin(\theta) r_c/2\pi$, and θ is the angle between the k mode of interest and the line of sight. Then the S/N of the cross power spectrum becomes similar to Equation (19) and needs to be replaced by the terms $P_{\rm cross}(k)$ and $\Delta P_{\rm cross}(k)$.

In Figure 8, we show the cross power spectra of Hα, [O III], [O II], and Hβ lines with the 21 cm line at $z = 1.0 \pm 0.2$. The errors are also shown for the CHIME and Tianlai experiments as solid and dotted bars, respectively. We find both the S/Ns of the cross power spectra for the CHIME and Tianlai are large enough to be well measured for all of the four lines at $z \sim 1$. The S/N of Tianlai is larger than that of CHIME, since it has greater collecting area, more receivers, and higher resolution,

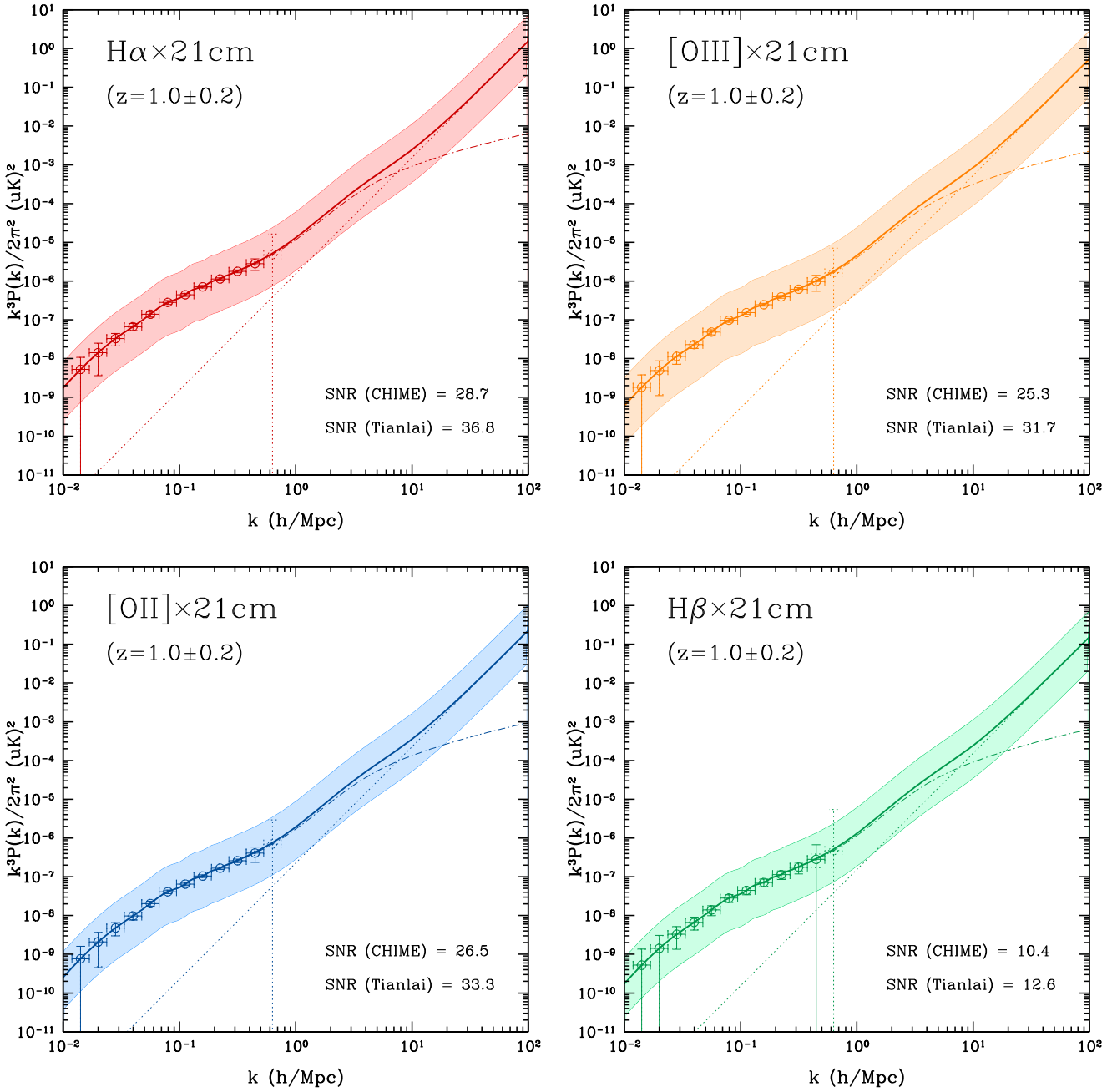

Figure 8. Cross power spectra of the Hα, [O III], [O II], and Hβ lines with the 21 cm line at $z = 1.0 \pm 0.2$. The errors for the CHIME and Tianlai experiments are shown as solid and dotted bars, respectively. The dashed–dotted and dotted curves denote the clustering and shot-noise terms of the cross power spectra, respectively. We find Tianlai has smaller errors and higher S/N than CHIME at a given redshift. Unlike the intensity power spectra probed by the SPHEREx, the 21 cm experiments are restricted by the relatively low spatial and spectral resolutions, and the cross power spectra can only be measured at large scales with $k < 1$ Mpc^{-1} h.

as shown in Table 3. Note that the measurable scales of the cross power spectrum are larger than the intensity power spectrum probed by SPHEREx alone (see Figure 6). This is because the spatial and spectral resolutions of CHIME and Tianlai are relatively low, so that only large scales with $k < 1$ Mpc^{-1} h can be detected. We find that the detectability of SPHEREx cross-correlated with CHIME or Tianlai is greatly improved compared to the current galaxy ×21 cm measurements given by Chang et al. (2010) and Masui et al. (2013). The S/N of SPHEREx×CHIME and Tianlai is ∼30 for the Hα, [O III] and [O II] lines, and it is ∼10 for the Hβ line at $z \sim 1$. For comparison, the S/N is less than 10 for the galaxy ×21 cm measurements at $z \sim 0.8$.

In Table 4, we tabulate the S/Ns of the cross power spectrum for the four optical lines with CHIME and Tianlai at $0.8 \leqslant z \leqslant 2.4$. As can be seen, the cross power spectra have large S/Ns over the redshift range, even for the relatively faint Hβ line with S/N > 5, and the foreground line contamination can be reduced significantly by cross-correlation. This indicates that cross-correlations of the four lines with the 21 cm line are an advantageous method for extracting the intensity fluctuation signal.

Another similar 21 cm experiment, the Hydrogen Intensity and Real-time Analysis eXperiment (HIRAX), focuses on the similar redshift range of $0.8 < z < 2.5$ as do CHIME and Tianlai for measuring BAO and constraining dark energy

Table 4
S/Ns for the Cross-correlations of Hα, [O III], [O II], and Hβ by SPHEREx with the 21 cm Line by CHIME and Tianlai at $0.8 \leqslant z \leqslant 2.4$

Line	21 cm expt.	$z = 1.0 \pm 0.2$	$z = 1.4 \pm 0.2$	$z = 1.8 \pm 0.2$	$z = 2.2 \pm 0.2$
Hα	×CHIME	28.7	26.9	18.9	15.2
	×Tianlai	36.8	36.1	26.6	22.0
[O III]	×CHIME	25.3	16.7	17.8	12.2
	×Tianlai	31.7	21.6	18.4	17.4
	×Tianlai	33.3	22.2	15.8	12.4
Hβ	×CHIME	10.4	6.8	7.8	5.2
	×Tianlai	12.6	8.5	10.5	7.3

(Newburgh et al. 2016). HIRAX is a new radio interferometer under development in South Africa, which is comprised of 1024 6 m parabolic dishes with frequency coverage of 400–800 MHz. It plans to observe 15,000 deg^2 with drift-scan mode in the Southern Hemisphere in four years. HIRAX can complement the observations of CHIME and Tianlai in the Northern Hemisphere, and provide additional measurements for BAO and LSS. The detectability of the cross power spectrum with HIRAX is similar to those of CHIME and Tianlai.

We can also estimate the detectability of cross power spectrum between SPHEREx and SKA phase one mid-frequency dish array (SKA1-mid).[15] SKA1-mid contains 190 15 m dishes and 64 MeerKAT dishes. Since SKA1-mid has relatively few short baselines, it has been proposed to use as a collection of single dishes for a large-scale intensity mapping survey (e.g., Bull et al. 2015). We adopt this strategy, and assume a system temperature $T_{\rm sys} = 25$ K and total integration time $t_{\rm tot} = 10^4$ hr for a total survey area $A_s = 10{,}000$ deg^2. A frequency resolution $\Delta\nu = 3.9$ kHz is adopted for SKA1-mid band one. We find the S/Ns of the cross power spectra between SPHEREx and SKA1-mid are lower than those for CHIME and Tianlai. For instance, S/N = 5.7 for Hα ×21 cm at $z = 1$, which is a factor of $5 \sim 6$ lower than for CHIME and Tianlai. This is basically due to the relatively low spatial resolution for SKA1-mid single dishes.

We need to note that the sensitivity estimates of the cross power spectra above are assuming perfect foreground subtraction. Imperfect subtraction, which can be caused by imperfect instrument modeling, will result in residual foregrounds as a noise in the observational data. This can significantly affect the measurements of cross power spectra, especially when considerable residual foregrounds are left in the data.

6. SFRD Constraints

The purpose of performing intensity mapping surveys is to illustrate the galaxy distribution, measure the BAO in the large-scale structure, and derive the statistical properties of galaxies and the universe. Some important quantities can be explored by intensity mapping, such as the SFRD (z), and cosmological parameters including Ω_M, Ω_Λ, dark energy equation of state w, σ_8, Hubble parameter H, and so on. In this section, using the Fisher matrix, we estimate the constraints on the SFRD available from emission line intensity mapping with SPHEREx. Accurate measurement of the SFRD is essential for studies of galaxy evolution, extragalactic background light, and other related fields, especially when including faint galaxies. Unlike the ordinary LF surveys by observing bright galaxies, intensity mapping could capture the emissions from faint galaxies, and provide more reliable constraints on the cosmic star formation history.

The Fisher matrix of the intensity mapping power spectrum $P(k)$ for two parameters q_i and q_j can be written as

$$F_{ij} = \sum_{k\ \rm bin} \frac{1}{\Delta P(k)^2} \frac{\partial P(k)}{\partial q_i} \frac{\partial P(k)}{\partial q_j}, \tag{27}$$

where $\Delta P(k)^2$ is the variance of the power spectrum. After obtaining the Fisher matrix, we can derive the covariance matrix of the parameters from $C_{ij} = (F^{-1})_{ij}$. For parameter errors without correlation, the covariance matrix is diagonal, and we can derive the error as $\sigma_i = \sqrt{F_{ii}^{-1}}$. In order to calculate the errors of the SFRD at different redshifts $\sigma_{\rm SFRD}(z)$, we set $q_{i,j} = {\rm SFRD}$, and estimate $\partial P(k)/\partial q$ in each k bin at a given redshift. The variance $\Delta P(k)^2$ can be obtained by Equation (16).

In Figure 9, we show the errors of the SFRD measured by SPHEREx, as estimated by the Fisher matrix. This result is derived from the Hα clustering power spectrum over $0.8 \leqslant z \leqslant 5.2$. We take the SFRD given in Hopkins & Beacom (2006) as the fiducial model. We find that the SFRD can be well constrained with an accuracy higher than 7% at $z \lesssim 4$. The error rises quickly at higher redshifts, since the S/N of the intensity power spectrum deceases significantly at high z. For the other lines, i.e., [O III], [O II], and Hβ, the constraints are not as good as for the Hα line, especially for the Hβ line. However, the [O III] and [O II] lines can still constrain the SFRD with good accuracy (<6%) at $z \lesssim 3$. These constraints are better than the ordinary method of measuring the LFs from individual galaxies. We can also make use of the cross power spectrum to measure the SFRD, which can suppress foreground line contamination. Intensity mapping surveys therefore offer an efficient way to probe the SFRD at different redshifts.

We notice that the Fisher matrix estimation actually produces the smallest errors for the parameters, and assumes a Gaussian probability distribution. There is also a degeneracy between the SFRD and other parameters, such as galaxy bias, which could enhance the uncertainty of the SFRD constraint. A more accurate and reliable method is to use the Markov chain Monte Carlo method to estimate the errors and include degeneracies between parameters. Besides the SFRD, we could also investigate constraints on cosmological parameters available from intensity power spectrum studies. We will discuss these in our future work.

[15] https://www.skatelescope.org/

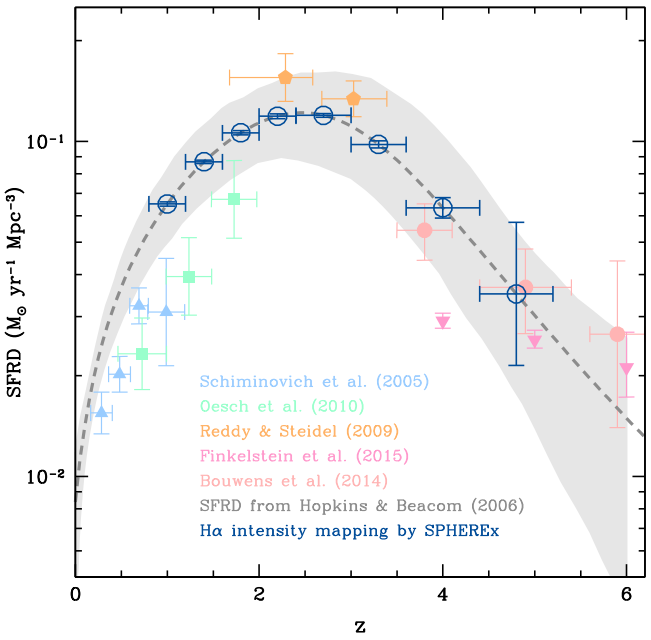

Figure 9. The constraints on the SFRD from the Hα intensity as measured by SPHEREx. The filled blue triangles, green squares, orange pentagons, red circles, and pink inverse triangles are the observational data given in other works (Schiminovich et al. 2005; Reddy & Steidel 2009; Oesch et al. 2010; Bouwens et al. 2014; Finkelstein et al. 2015). The gray curves show the SFRD given in Hopkins & Beacom (2006), and the gray region shows the 2σ C.L. We find that intensity mapping can provide stringent constraints on the SFRD at $z \lesssim 4$.

7. Summary and Discussion

In this work, we investigated intensity mapping of the Hα, [O III], [O II], and Hβ lines at $0.8 \leqslant z \leqslant 5.2$. We first estimated the mean intensities of the four optical emission lines at different redshifts using three methods, i.e., the observed LFs, simulations of the galaxy SFR, and SFRD(z) derived from observations. We find the results of the three methods are consistent with one another at the 1σ C.L. for all four lines. We also have taken account of dust extinction in the estimates, so that the mean intensities we obtain are the observed ones.

Besides the mean intensity, the fluctuation of the intensity is the main focus of our study. We calculate the intensity power spectra for the four lines using a halo model at $0.8 \leqslant z \leqslant 5.2$. We find that the power spectra have similar amplitudes at $1 \lesssim z \lesssim 2$ due to the increasing SFRD and bias over this redshift range. The intensity power spectrum drops significantly at $z \gtrsim 3$. This implies that it is challeging to measure the intensity power spectrum at high redshifts, although we can make strong detections at $z < 3$.

Foreground line contamination is important to intensity mapping surveys. We assume there is no large foreground contamination for the Hα line, though [O III], [O II], and especially Hβ are more challenging. We explored flux cuts that can suppress foregrounds by approximately one order of magnitude below the signal for the [O III], [O II], and Hβ lines. The [O III] and [O II] lines have similar flux cut thresholds at low redshifts, and both are larger than those of the Hβ line.

In order to study the detectability of the intensity power spectra of the four lines, we take the proposed SPHEREx experiment as an example to evaluate errors and S/Ns. As expected, Hα has the highest S/Ns at all redshifts with S/N > 7 at $z \lesssim 4$. The S/Ns of the [O III] and [O II] are also as high as S/N > 8 at $z < 3$, and <3 for the Hβ line over the redshift range of interest. We also estimate the percentage of the SPHEREx survey voxels that need to be masked to suppress foregrounds. We find this percentage is less than $\sim$10% and 30% for the [O III] and [O II] lines, respectively, at $z < 3$, which indicates that it is feasible to mitigate the foregrounds for the [O III] and [O II] lines.

Another method to reduce the foreground contamination is to cross-correlate two lines at the same redshift. We investigate the cross-correlations of the 21 cm line measured by the CHIME and Tianlai experiments with the four optical lines probed by SPHEREx at $0.8 \leqslant z \leqslant 2.4$. We find that the S/Ns of the cross power spectra are large enough to detect all four lines, even for the relatively faint Hβ (which gives S/N > 5 at $z < 2.4$). This suggests that the cross correlation of optical lines with the 21 cm line provides a reliable way to extract the signals.

Finally, we predict the constraints on the SFRD (z) from the intensity mapping of the Hα, [O III], [O II], and Hβ lines with SPHEREx. The Fisher matrix is used to generate our prediction, and we find the intensity mapping can provide a stringent constraint on the SFRD at $z \lesssim 4$. The accuracy is higher than 7% at $z \lesssim 4$ for Hα intensity mapping, and higher than 6% for [O III] and [O II] at $z \lesssim 3$. This constraint is tighter than the ordinary method of LF measurements from individual galaxies. Besides constraining the SFRD, intensity mapping also can constrain the properties of dark matter, dark energy, and cosmological parameters, since it captures the evolution of the large-scale structure of the universe. We expect that intensity mapping will have an increasingly important role in studies of galaxy evolution and cosmology in the future.

Y.G. acknowledges the support of Bairen program from the National Astronomical Observatories, Chinese Academy of Sciences. Y.G. thanks Qi Guo for helpful discussion about the simulation results. Y.G. and A.C. acknowledge the support from NSF CAREER AST-0645427 and AST-1313319, and the NASA grants NNX16AF39G and NNX16AF38G. M.B.S. thanks the Netherlands Foundation for Scientific Research support through the VICI grant 639.043.006. C.F. acknowledges support from NASA grants NASA NNX16AJ69G and NASA NNX16AF39G. M.G.S. acknowledges support from South African Square Kilometre Array Project and National Research Foundation. X.L.C. acknowledges the support of the MoST 863 program grant 2012AA121701, the CAS Strategic Priority Research Program "The Emergence of Cosmological Structures" XDB09020301, and the NSFC through grant No. 11373030. Part of the research described in this paper was carried out at the Jet Propulsion Laboratory, California Institute of Technology, under a contract with the National Aeronautics and Space Administration.

References

Arendt, R. G., Kashlinsky, A., Moseley, S. H., & Mather, J. 2016, ApJ, 824, 26
Baldry, I. K., & Glazebrook, K. 2003, ApJ, 593, 258
Bayliss, K. D., McMahon, R. G., Venemans, B. P., Ryan-Weber, E. V., & Lewis, J. R. 2011, MNRAS, 413, 2883
Bouwens, R. J., Bradley, L., Zitrin, A., et al. 2014, ApJ, 795, 126
Bull, P., Ferreira, P. G., Patel, P., & Santos, M. G. 2015, ApJ, 803, 21
Calzetti, D., Armus, L., Bohlin, R. C., et al. 2000, ApJ, 533, 682
Carilli, C. L. 2011, ApJL, 730, L30
Chang, T.-C., Pen, U.-L., Bandura, K., & Peterson, J. B. 2010, Natur, 466, 463
Colbert, J. W., Teplitz, H., Atek, H., et al. 2013, ApJ, 779, 34
Cole, S., Norberg, P., Baugh, C. M., et al. 2001, MNRAS, 326, 255

Cooray, A., & Sheth, R. 2002, PhR, 372, 1
Cooray, A., Smidt, J., De Bernardis, F., et al. 2012b, Natur, 494, 514
Dore, O., Bock, J., Ashby, M., et al. 2015, arXiv:1412.4872
Finkelstein, S. L., Ryan, R. E., Jr., Papovich, C., et al. 2015, ApJ, 810, 71
Fonseca, J., Silva, M., Santos, M. G., & Cooray, A. 2016, arXiv:1607:05288
Gong, Y., Chen, X., Silva, M., Cooray, A., & Santos, M. G. 2011a, ApJL, 740, L20
Gong, Y., Cooray, A., Santos, M., et al. 2012, ApJ, 745, 49
Gong, Y., Cooray, A., & Santos, M. 2013, ApJ, 768, 130
Gong, Y., Cooray, A., Silva, M. B., Santos, M. G., & Lubin, P. 2011b, ApJL, 728, L46
Gong, Y., Silva, M., Cooray, A., & Santos, M. G. 2014, ApJ, 785, 72
Guo, Q., Simon, W., Raul, E. A., et al. 2013, MNRAS, 428, 1351
Hayashi, M., Sobral, D., Best, P. N., Smail, I., & Kodama, T. 2013, MNRAS, 430, 1042
Hopkins, A. M., & Beacom, J. F. 2006, ApJ, 651, 142
Kennicutt, R. C. 1998, ARA&A, 36, 189
Khostovan, A. A., Sobral, D., Mobasher, B., et al. 2015, MNRAS, 452, 3948
Komatsu, E., Smith, K. M., Dunkley, J., et al. 2011, ApJS, 192, 18
Lidz, A., Furlanetto, S. R., Oh, S. P., et al. 2011, ApJ, 741, 70
Lidz, A., & Taylor, J. 2016, arXiv:1604.05737
Ly, C., Malkan, M. A., Kashikawa, N., et al. 2007, ApJ, 657, 738
Madau, P., & Dickinson, M. 2014, ARA&A, 52, 415
Masui, K. W., Switzer, E. R., Banavar, N., et al. 2013, ApJL, 763, L20
McQuinn, M., Zahn, O., Zaldarriaga, M., Hernquist, L., & Furlanetto, S. R. 2006, ApJ, 653, 815
Mitchell-Wynne, K., Cooray, A., Gong, Y., et al. 2015, NatCo, 6, 7945
Newburgh, L. B., Bandura, K., Bucher, M. A., et al. 2016, Proc. SPIE, 9906, 99065X
Oesch, P. A., Bouwens, R. J., Carollo, C. M., et al. 2010, ApJL, 725, L150
Osterbrock, D. E., & Ferland, G. J. 2006, Astrophysics of Gaseous Nebulae and Active Galactic Nuclei (Mill Valley, CA: Univ. Science Books)
Pullen, A., Dore, O., & Bock, J. 2014, ApJ, 786, 111
Reddy, N. A., & Steidel, C. C. A. 2009, ApJ, 692, 778
Schechter, P. 1976, ApJ, 203, 297
Schiminovich, D., Ilbert, O., Arnouts, S., et al. 2005, ApJL, 619, L47
Sheth, R. K., & Tormen, G. 1999, MNRAS, 308, 119
Silva, M., Santos, M. G., Cooray, A., & Gong, Y. 2015, ApJ, 806, 209
Silva, M., Santos, M. G., Gong, Y., Cooray, A., & Bock, J. 2013, ApJ, 763, 132
Sobral, D., Matthee, J., Best, P. N., et al. 2015, MNRAS, 451, 2303
Sobral, D., Smail, I., Best, P. N., et al. 2013, MNRAS, 428, 1128
Uzgil, B. D., Aguirre, J. E., Bradford, C. M., & Lidz, A. 2014, ApJ, 793, 116
Visbal, E., & Loeb, A. 2010, JCAP, 11, 016
Yue, B., Ferrara, A., Pallottini, A., Gallerani, S., & Vallini, L. 2015, MNRAS, 450, 3829
Zemcov, M., Smidt, J., Arai, T., et al. 2014, Sci, 346, 732